Journal Pre-proofs

Fast and inexpensive emission-time *in-situ* setup for upconversion nanoparticle characterization

Mirta R. Alcaraz, Cecilia Sorbello, Loreiny Parra Florez, Roberto Etchenique

PII: S0026-265X(23)00969-4
DOI: https://doi.org/10.1016/j.microc.2023.109350
Reference: MICROC 109350

To appear in: *Microchemical Journal*

Received Date: 22 July 2023
Revised Date: 9 September 2023
Accepted Date: 9 September 2023

Please cite this article as: M.R. Alcaraz, C. Sorbello, L.P. Florez, R. Etchenique, Fast and inexpensive emission-time *in-situ* setup for upconversion nanoparticle characterization, *Microchemical Journal* (2023), doi: https://doi.org/10.1016/j.microc.2023.109350

Rev_MICROC-D-23-02833_Highlighted

Fast and inexpensive emission-time *in-situ* setup for upconversion nanoparticle characterization

Mirta R. Alcaraz[1,2,3,], Cecilia Sorbello[2,3], Loreiny Parra Florez[2,3], Roberto Etchenique[2,3,*].*

[1] Laboratorio de Desarrollo Analítico y Quimiometría (LADAQ), Cátedra de Química Analítica I, Facultad de Bioquímica y Ciencias Biológicas, Universidad Nacional del Litoral, Ciudad Universitaria, Santa Fe (S3000ZAA), Argentina.

[2] Departamento de Química Inorgánica, Analítica y Química Física, INQUIMAE, Facultad de Ciencias Exactas y Naturales, Universidad de Buenos Aires, Intendente Güiraldes 2160, Ciudad Universitaria, Pabellón 2, Buenos Aires (C1428EGA), Argentina.

[3] Consejo Nacional de Investigaciones Científicas y Técnicas (CONICET), Godoy Cruz 2290, Buenos Aires (C1425FQB), Argentina.

CORRESPONDING AUTHORS

malcaraz@fbcb.unl.edu.ar Tel: 54 342 4575206x190 (M.R. Alcaraz)

rober@qi.fcen.uba.ar Tel: 54 11 52858570 (R. Etchenique)

ABSTRACT

In this work, a straightforward analytical approach is presented for the evaluation of the entire time-resolved emission spectrum of Er^{3+}-doped upconversion nanoparticles (UCNP) by the acquisition of bidimensional emission wavelength-time signals. Employing diffractive optics and fast optomechanical sweeping, the entire emission wavelength-time matrix (EtM) of UCNP is registered. An optic fibre probe allows the measurement of micrometric-size domains in surfaces, either in solid form or in suspension. Further chemometric analysis was also performed to gain further insight into the behaviour of the emission bands and their corresponding time curve profiles. To show the applicability of the developed procedure, changes either in the emission spectrum or the time behaviour by external perturbations were monitored and EtM at different temperatures was acquired as a proof of concept. The results demonstrated the effectiveness of the proposed procedure in obtaining fast and highly informative images and enlightening knowledge about the phosphorescence-based system.

KEYWORDS: phosphorescence sensors, emission wavelength-time imaging, chemometrics, instrumental setup

1. INTRODUCTION

The accelerated growth of the nanotechnology interest can be attributed to the convergent evolution of nanosized materials and emerging technologies, such as biotechnology, biomedical engineering, and artificial intelligence, among others. These materials are intentionally produced on a nanoscale, providing them with unique properties that are not available on the bulk scale. [1] Over the last decade, different types of nanomaterials, particularly nanoparticles (NPs), have been synthesized from metals, nonmetals and oxides, and varied structures, shapes, sizes, and compositions were manufactured. [2] For instance, Ag NPs are uniform particles constituted by only one type of material, whereas some NPs consist of a core/shell structure. [2] This variety of composition confers them a full breadth of compatibility with different media and systems, spanning its application from biological, cosmetic, energetic, environmental, and biomedical fields, and others.

Upconverting NPs (UCNPs) are a group of lanthanide-doped nanosized particles that realize non-linear photo upconversion of infrared (IR) excitation with an extensive anti-Stokes shift. [3] These particles have extraordinary chemical stability. Capitalizing on its intrinsic attributes, this type of NPs is presented as a promising candidate for biomedical application, especially, in theragnostic. In this regard, the use of near-IR excitation light has the advantage of deeper tissue penetration with minimum photodamage effects and shows the benefit of reducing light scattering, phototoxicity, and autofluorescence. [4] The most common design of UCNPs is the core/shell structure that has the advantage of leveraging photoluminescence efficiency. [5]

While research and development of different UCNPs are active topics worldwide with numerous publications in the relevant literature, there is still a dearth of comprehensive understanding regarding some of its properties.

The most reported applications of UCNPs are based on the variation of the intensity and frequency of the emission signals. Notwithstanding, a new topic of research is focused on the kinetics of upconversion luminescence (UCL). The time-domain evaluation of the UCL allows for exploiting a new dimension of the UC emission, which expands its use for manifold applications, including anti-counterfeiting technologies. [6–8]

The control of luminescence kinetic parameters in UCNPs is crucial for their effective use in microscopies. Although long intermediate state lifetimes facilitate the excitation of higher states using low-intensity light, they also limit the high emission fluence necessary for bright imaging. Furthermore, a saturation of intermediate states causes excitation to behave linearly, which prevents one of the most interesting features of multiphotonic excitation: the ability to perform z-sectioning. [9]

In this work, a straightforward inexpensive spectrometer setup is introduced for the evaluation of the photoluminescence time profile of UCNPs at the entire UC spectrum. The proposed setup allows the simultaneous registering of the UC spectrum and the temporal changes at each wavelength, obtaining a bi-dimensional data matrix. In addition, its applicability in luminescence thermometry experiments is demonstrated. The obtained data were further analyzed through chemometric techniques allowing extraction of the most relevant information of the system under study and the results were compared with those obtained from the classical analysis.

2. EXPERIMENTAL SECTION

2.1. Reagents and solutions.

Yttrium (III) acetate tetrahydrate ($Y(CH_3COO)_3 \cdot 4H_2O$, 99.9%), ytterbium (III) acetate tetrahydrate ($Yb(CH_3COO)_3 \cdot 4H_2O$, 99.9%) and erbium (III) acetate tetrahydrate ($Er(CH_3COO)_3 \cdot 4H_2O$, 99.9%) were purchased from Alfa-Aesar (Massachusetts, United State of America) and used as received. Ammonium fluoride (NH4F ≥ 99.99%), 1–octadecene (90%), and oleic acid (OA, 90%) were purchased from Sigma-Aldrich (Argentina). Sodium hydroxide (NaOH, 99%) and LC methanol (MeOH) were purchased from Merck (Argentina). Cyclohexane (cHex, technical grade) and absolute ethanol (EtOH, 99.5%) were acquired from Sintorgan (Argentina) and Ciccarelli (Argentina), respectively.

2.2. Core-shell UCNP synthesis.

The Er-doped core-shell UCNPs were synthesized as reported elsewhere following the so-called oxygen-free protocol. [1,10–13] To put it succinctly, $NaYF_4$:Yb,Er cores were synthesized by mixing the appropriate amount of lanthanide acetates with 6 mL of OA and 15 mL of 1–octadecene. This mixture was stirred and heated at 120 °C in N_2 atmosphere and kept for 30 min under a vacuum. The clear mixture was then cooled to 50 °C and an NH_4F/NaOH methanolic solution was rapidly added and kept for 30 min under N_2 atmosphere. Immediately after, MeOH was removed by vacuum evaporation. The resultant pale-yellow mixture was heated under an N_2 atmosphere using a ramp of 15 °C/min until reached 315 °C and kept for 90 min. After cooling it to room temperature absolute EtOH was added in excess and the particles were centrifuged at 5000 g for 20 min. The supernatant was discarded, the precipitate was redispersed in 3 mL of cHex, and an excess of EtOH was again added to precipitate the particles; the mixture was then centrifuged at 5000 g for 20 min. The 2-step purification cycle was repeated twice. Finally, the obtained oleic-modified cores were redispersed in 7.5 mL of cHex. To deposit the $NaYF_4$ shell over the $NaYF_4$:Yb,Er cores a similar procedure as described for the UCNP core synthesis was employed. The resultant $NaYF_4$:Yb,Er@$NaYF_4$ UCNPs were used as synthesized. (For more details, the reader is referred to the specific literature). [5,13]

The synthesized UCNPs were characterized through X-ray diffraction (XRD) and scanning electron microscope (SEM). The XRD signal and the SEM images are shown in Figures S-1 and S-2 (supplementary information), respectively.

2.3. Experimental setup for emission wavelength-time matrix measurements.

The illustrative diagram of the developed spectrometer is depicted in Figure 1. A pulsed 10 mW (average power) 980 nm laser diode (1) is used to excite the upconversion emission of the UCNP in the sample (7). The NIR light is collimated and directed (2, 3, 4) through a multimode optical fibre to the sample (5, 6). Its UC emission is collected

back to a dichroic mirror (4), which deflects it toward a single-axis galvo (10). A ramp generator triggered with the onset of the laser pulses drives the single-axis galvo (Fig.1 inset) configuring a linear sweeping used for the time-to-position conversion in one of the image dimensions. At about half of the total deflection, the laser is turned off to image both the onset and the time-resolved signal. A transmission diffraction grating (11) at 90° from the galvo movement separates the different colours of the UC emission. Finally, the UC emission wavelength-time matrix (EtM) is collected by a CMOS camera (12) (Point Grey, Flea 2, FL2G-13S2M-C), which was directly read by a computer via a Firewire interface.

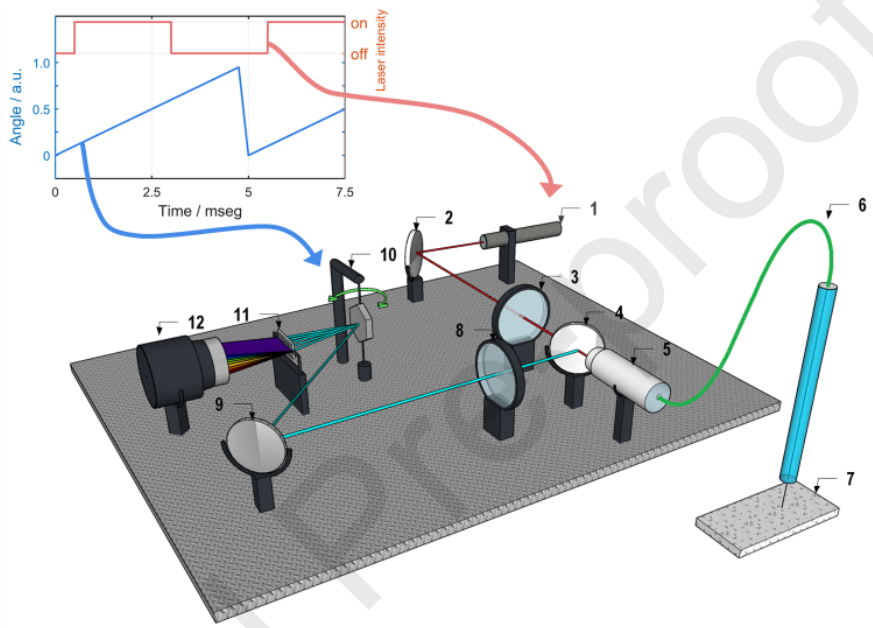

Figure 1. Illustrative diagram of the experimental setup for the emission-time matrix acquisition of UCNP. 1) 980 nm laser diode, collimated (10 mW); 2) XY adjustable mirror; 3) lens (fd = 30 mm); 4) Dichroic mirror, long pass beam-splitter (cut-off wavelength = 750 nm); 5) optical fibre connector. 6) 62.5 nm multimode optical fibre; 7) sample; 8) lens (fd = 30 mm) + short-pass filter (800 nm); 9) XY adjustable mirror; 10) single axis galvo; 11) diffraction grating; 12) CMOS camera (Point Grey, Flea 2, FL2G-13S2M-C)

The setup was mounted on a breadboard over a Styrofoam cushion to minimize vibrations. The optical fibre (~ 50 cm length) was directed to the sample, which can be placed onto a computer-controlled thermostatic surface.

Wavelength calibration was done by analytical inspection of an image obtained for a 2% Er^{3+} doped UCNP sample and by direct comparison with the known emission lines of Er^{3+} in fluoride-containing lattices; then, a linear fitting was carried out to obtain the continuous wavelength range. Time calibration was performed utilizing an *ad-hoc* LED driver oscillator, which was previously calibrated by using an oscilloscope (UNI-T, UTD2102CEX, 100MHz, 1GS/s). To prevent changes in the instrument scale, both

wavelength and time axis calibration were performed immediately before the measurements.

2.4. Temperature-dependence analysis.

EtM were sequentially collected in the temperature range of 297-367 K at ~2 K intervals. In this way, a total of 340 matrices were acquired. For the measurement, the sample was dropped in a conductive plate until dryness; then, the sample was allowed to dwell for at least 10 min at the initial temperature (297 K).

2.5. Data generation and software.

The EtM imaging was acquired as a 16-bit image and saved in tiff format using FlyCapture 2 Viewer. All the images were analyzed with ImageJ software, which is freely available at https://imagej.nih.gov/ij/download.html. For further data evaluation and analysis, the tiff images were eventually converted to double-precision data by using the im2double MATLAB function. Data processing and analysis were performed in MATLAB 2015b. [14] MCR-ALS GUI 2.0[15] codes for MATLAB were freely downloaded from www.mcr-als.info.

3. RESULTS

3.1. General considerations.

Lanthanide-doped NPs can convert long-wavelength light, mainly NIR (>900 nm), to shorter wavelengths, such as visible red, green, and, in some cases, blue light. This UC phenomenon is the consequence of a two-photon (in some cases, three-photon) process that occurs via energy transfer from Yb^{3+} ions to Er^{3+} ions. Yb^{3+} ions act as sensitizers via the $^2F_{7/2}$ (fundamental state) → $^2F_{5/2}$ (excited state) transition. The latter is resonant in energy with the $^4I_{11/2}$ state of $Er^{3+,}$ which is an intermediate state in the two-photon process. Hence, the Er^{3+} is excited to the $^4F_{7/2}$ state by a two-step energy transfer from the excited Yb^{3+} ion. Succeeding nonradiative processes within Er^{3+} ions populate the radiating states. The characteristic strong emission bands of Er^{3+} arise at *ca*. 660 nm, 548 nm, 525 nm, and 408 nm, corresponding to the $^4F_{9/2} \rightarrow {}^4I_{15/2}$, $^4S_{3/2} \rightarrow {}^4I_{15/2}$, $^2H_{11/2} \rightarrow {}^4I_{15/2}$, and $^2H_{9/2} \rightarrow {}^4I_{15/2}$, respectively. [9,16] A level energy diagram of the most relevant energy transitions in the upconverting process is depicted in Figure S-3 (supplementary information).

In particular, the green emission bands rising from the transition of $^2H_{11/2}$ and $^4S_{3/2}$ excited states are near and, hence, they are in thermal equilibrium governed by a Boltzmann distribution, as it was stated by Savchuk *et al.* who used equation (1) to describe the model: [17]

$$\frac{I_{525}}{I_{550}} = C \times \exp\left(-\frac{\Delta E}{k_B T}\right) \quad (1)$$

where I_{525} and I_{550} are the intensity of the $^2H_{11/2} \rightarrow {}^4I_{15/2}$ and $^4S_{3/2} \rightarrow {}^4I_{15/2}$ transitions, respectively; C comprises degeneracy spontaneous emission rate and absorption rates; ΔE is the energy gap between the two thermally coupled energy levels involved in the radiative transitions; k_B is the Boltzmann constant, and T is the absolute temperature. [17–19] Hence, it is possible to evaluate the capability of the UCNPs as temperature sensors by analysing changes in the emission intensity ratio. [10,19]

On the other hand, the time-decay (τ) of the emitting levels implies thermometric information. Methods based on time-decay measurements utilize a pulsed excitation source; after each excitation pulse, the emitting levels show an emission decay behaviour characterized by temperature dependence as follows:

$$\tau = \frac{1}{\tau_0^{-1} + k\exp\left(-\frac{\Delta E}{k_B T}\right)} \quad (2)$$

where τ_0^{-1} is the radiative lifetime at absolute zero temperature and k is a pre-exponential factor (k_B, ΔE, and T are the same as Eq. 1). Therefore, UCNPs can be used as a temperature sensor by evaluating variations in the decay profile or the τ value. It is important to note that although, in principle, the population mechanism of the emissive states allows the appearance of more complicated behaviours, in the analysed samples all decays were monoexponentially fitted.

3.2. Optical characterization of the setup.

To make the EtM images usable for general purposes, calibration of both wavelength and time axis was required. For wavelength calibration, several procedures were tested. Considering that Er^{3+} transitions in fluoride lattices were profusely studied and their wavelengths are well established in the literature, [20–23] the tabulated energy of Er^{3+} transitions was used for calibration because of its simplicity and robustness. Using this procedure, a good linear relationship between pixel number (pix#) and wavelength (λ) was obtained. Depending on the exact optical path and the used sensor, a relationship of about 0.5 nm to 0.7 nm/pix# was chosen. In a typical measurement, the relationship λ (nm) = 677.100 – 0.586 × pix# was implemented. For comparison, alternative calibration procedures based on the signal analysis of LEDs and laser diodes were also utilized, obtaining comparable results (± 1.3 nm). The typical resolution of the spectral bands, measured at the $^4F_{7/2}$ band emission (or an alternative laser diode source at 635 nm), was 3.8 nm FWHM. This resolution can be enhanced by diminishing the secondary image of the optical fibre end but at the cost of obtaining a darker image.

On the other hand, despite its simplicity, calibration of the time axis using the characteristic times-decay of UC emission bands was not possible. Different Er^{3+} concentrations, matrices, environments, and even different batches of UCNPs synthesized under identical conditions show an important dispersion of time-decay, probably due to different decay paths and quenching mechanisms. Therefore, the calibration was done utilizing an astable multivibrator that switches an LED on/off with a period of 234 μs. This multivibrator was previously calibrated with an oscilloscope, detected by the optical fibre end (Figure S-4). As expected from the mechanism of the time-image generator, the relationship between pix# and time was linear in the 100s of microsecond range. On the assumption that this linearity extends to the pixel size, a factor of 22.776 μs/pix# was determined. The scaling can be chosen by varying the galvo mirror oscillation frequency, accommodating wide scales of time ranging from 200 μs and 10 ms. This characteristic allows the use of the device for different timescales of population and decay of emitting materials. Although the accuracy of the analogue signal can be improved, the time digitization, determined by the finite number of pixels, led to a time resolution of 1/300-1/600 of the total period. This resolution range (0.33 – 33 μs) allows the proper measurement of most lanthanide-based upconversion materials and other analytes with emission in the range of μs to ms.

In the context of a spatial imaging device, the pseudo-Point Spread Function (p-PSF) describes the response of the system to a point source of light. In thi particular device, one of the spatial axes corresponds to wavelength, while the other represents the time. To assess the data precision, a measurement of the p-PSF was performed utilizing a monochromatic laser emitting at 454 nm, pulsed to capture a "time-point" of 5 μs, a duration smaller than a single pixel on the chosen scale. The results are shown in Figure S-5, Supplementary Information. The p-PSF features like an assimetric distorted Gaussian spot, comprising approx. 4 pixels (2.1 nm, FWHM) and 4.8 pixels (33 μs) in the wavelength and time scales, respectively. The spread of the p-PSF also serves as indicator of the minimal crosstalk between modes that would be expected in a given image. As the time axis can be swept up to 5 times faster than this particular measurement, a 7 μs time precision can be achieved, at the cost of a shorter time span for the whole image. Different relationships between the span of time and wavelength could be obtained also by changing the optical path between collecting lens (8 in Figure 1) and galvo (10 in Figure 1), or the groves/mm of the grating (11 in Fugure 1), respectively.

Figure S-6 shows a 32-bit EtM image of a sample containing 2% Er^{3+} doped UCNPs deposited onto a cover glass and excited at 980 nm (Some spectral regions of the image were digitally magnified to facilitate its visual inspection). The emission spectrum acquired at a specific time pulse is also depicted, indicating the known Er^{3+} transitions. All the transitions are from the labelled to the fundamental level ($^4I_{15/2}$), except the line near 470 nm, which corresponds to the $^2P_{3/2} \rightarrow {}^1I_{11/2}$ transition. Most of the transitions are split and/or appear broad because Er^{3+} can occupy several different sites in the crystal lattice. [20,21,23]Most of the publications of UCNP studies evaluate only the red and green emission bands, which correspond to the emission from $^4F_{9/2}$, $^2H_{11/2}$, and $^4S_{3/2}$ levels. [24–26] Some of them may include the blue band of the emission from $^2H_{9/2}$. [22] However, emissions from $^4F_{7/2}$, $^4F_{3/2}$, $^4F_{5/2}$, $^2P_{3/2}$, and $^4G_{11/2}$ are seldom shown because of their weakness, which is usually beyond the capability of the measurement systems, although they have been studied. Tallant et al. have described and analyzed the transitions from $^4F_{7/2}$, $^4F_{5/2}$and $^4G_{11/2}$ to the ground state, [20] while Dammak has described the weaker $^4F_{3/2}$. [27] On the other hand, Gaebler et al. have reported the transition from $^2P_{3/2}$

to the intermediate level $^4I_{11/2}$, around 470 nm. [28] Notably, in the present case, using a standard 16-bit imaging mode, emission lines with intensities ranging within 3 orders of magnitude were easily resolved (Figure S-5). This outcome represents an outstanding step forward in the field of UCNP characterization. On the other hand, faster measurements can be performed with 8-bit imaging mode with excellent results in case precise measurements on the individual weak transitions are not required.

To obtain these images, a CMOS camera (Point Grey FL2G-13S2M-C) was used, albeit several cameras were tested with similar results. Big sensors are advantageous since the spectral and temporal span can increase. Noise and Quantum Yield (QY) are the main features to consider in improving some analytical figures of merit, such as limit of detection (LOD) and analytical sensitivity.

The speed of imaging acquisition is another crucial aspect to consider when monitoring a dynamic process. Although UC EtM can be obtained using commercial setups in sequential mode, the procedure can be tedious and fast results are difficult to combine with high throughput data. The measurement of kinetic parameters can be done in different ways. For instance, direct analysis of single-wavelength kinetics is straightforward, although time-consuming when a complete matrix of emission wavelength-time is required. [9] On the other hand, a streak camera can be utilized to obtain the EtM. Even though this approach can be used as multilinear input for chemometric analysis, the equipment costs increase in orders of magnitude. [29] In 2016, an inexpensive and clever alternative was proposed by Zhu, [30] in which a smartphone camera takes an image in a rotating platform. This strategy has the particularity of gathering only three points in the spectral mode, which, albeit interesting, restrains the analytical performance in terms of selectivity when complex systems are under study. High acquisition rate is essential to avoid crosstalk between modes and ensure mode independence when high-order data undergo chemometric resolution.

Last, the procedure proposed in this work significantly reduces costs. The total cost for the setup depicted in Figure 1 was less than USD 1500, an order of magnitude lower than any available equipment in the market. Depending on the specific needs, different parameters, such as wavelength, time, speed, noise, quantum yield, and price, can be prioritized and customized accordingly.

3.3. Evaluation of the emission time profile and the UC emission.

A double-precision EtM obtained from an 8-bit resolution image is shown in Figure 2, indicating the emission time profile and the UC emission spectrum subtracted from the original data matrix.

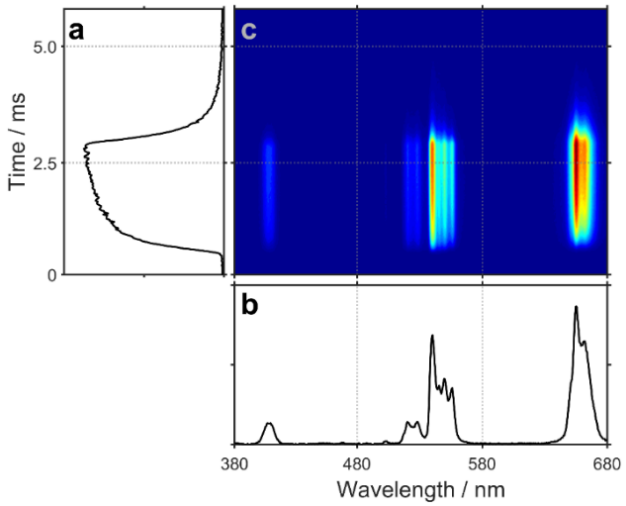

Figure 2. EtM acquired with the experimental setup at room temperature (297 K). a) Photoluminescence time profile at 540 nm. b) UC emission spectrum acquired at the end of the excitation pulse. c) bidimensional EtM.

The acquired matrices are 256 × 512 bidimensional data arrays comprising the time profile of luminescence, with the rise and the decay process, and the emission spectra under excitation at 980 nm, respectively. The time profile corresponds to an excitation pulse of 2500 μs length. The time profile shows the characteristic feature of the lanthanide phosphorescence rise-decay curve. [7,9]

To comprehend the decay behaviour of the UC emission at room temperature (297 K), τ at the most significant wavelength was calculated by fitting the decay curves with mono-exponential models, according to

$$y = y_0 + A\exp\left(-\frac{t}{\tau}\right) \quad (3)$$

where y_0 and A are empirical constants and t is the measured time in ms. All the fitted models were assessed by Chi-squared goodness-of-fit tests, which satisfied the tolerance criterion in all cases. From this analysis, three different τ-values can be distinguished: 1) 0.37±0.01 ms, characteristic of the red emission; 2) 0.29±0.01 ms, mostly for green emission bands; and 3) 0.20±0.01 ms, for the shorter τ associated with the blue emission. (For more details, the reader must refer to Table S-1, Supplementary information). These results are aligned with those reported in the literature for the same type of UCNPs. [22] It should be highlighted that, even though they are detected, τ-values of $^4F_{7/2}$, $^4F_{5/2,}$ and $^4G_{11/2}$ emission bands could not be estimated because of the low signal-to-noise ratio due to the 8-bit depth of the original images.

To gain further insight into the behaviour of the emission bands and their corresponding time curve profiles, the EtM was subjected to multivariate curve resolution-alternating least square (MCR-ALS) decomposition. MCR-ALS is a soft-modelling algorithm that enables unravelling the individual profiles of overlapped signals

in a bilinear data matrix, providing comprehensive and meaningful models with chemically interpretable outputs.[31,32] This particularity, in combination with its flexibility, makes MCR-ALS a compelling tool for the analysis of complex systems, and as a matter of fact, it has been widely implemented in uncountable applications with quantitative and qualitative aims. [33–36] Capitalizing on the ability to decompose bi-dimensional data matrices without requiring any known information about the system, or minimal information if available, MCR-ALS seems to be the best candidate to unravel the spectral and luminescence time behaviour in the present system.

For the resolution, a SIMPLISMA-like methodology [37,38] was utilized to extract the initial estimates in the time dimension and the number of components was estimated through singular value decomposition (SVD) and principal component analysis (PCA). Three components were necessary to explain the system. In the iterative step, nonnegativity in both modes was imposed as a constraint.

Figure 3 shows the overall emission spectrum (a) and the emission time profiles extracted from the different emission bands (b) at which τ-values were estimated, as well as the profiles retrieved from MCR-ALS (c-d).

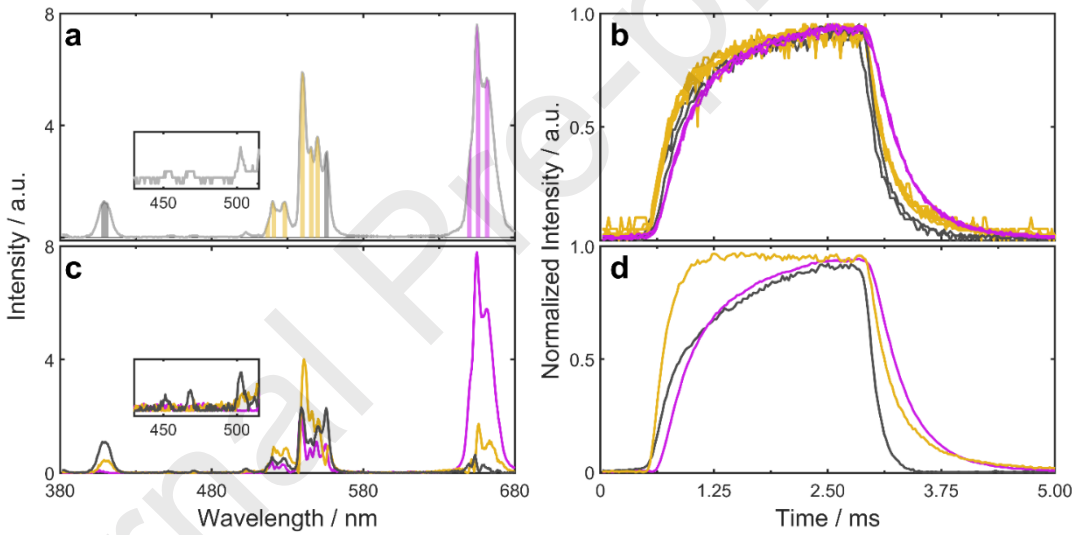

Figure 3. a) UC emission spectrum indicating the bands at which the τ-values were estimated and b) the corresponding time curves (magenta: 0.37±0.01 ms, orange: 0.27±0.01 ms, black: 0.20±0.01 ms). c) Spectral and d) time profiles retrieved from MCR-ALS (magenta: 0.38 ms, orange: 0.30 ms, black: 0.14 ms). Inset: amplified section of the raw emission spectrum (a) and the retrieved spectral profiles (c) in the region between 420-515 nm. The measurement was performed at 297 K. (Colour should be used in the print version)

These results show that the photoluminescence of the UC emission bands can decay from different pathways. The most relevant outcome is the fact that emission bands are a collection of several bands that behave differently. This evidence led to the conclusion that the τ-values calculated following the classical procedure (at one specific emission band) would be a combination of time-decays (for more information, the reader referred

to Table A-1, Supplementary Information). For quantitative comparison, τ-values were estimated using the time curve profiles retrieved from MCR-ALS by following the same procedure as described before. These values were: 0.38 ms, 0.30 ms, and 0.14 ms. As can be appreciated, slight differences were obtained for the longer lifetimes (0.38 ±0.01 ms and 0.29±0.01 ms, respectively), whereas the shorter (0.14±0.01 ms) was significantly lower than those obtained before (0.20±0.01 ms). This outcome is of great importance since it made it possible to unveil the lifetime of $^4F_{7/2}$ and $^4F_{5/2}$ to the fundamental state and $^2P_{3/2} \rightarrow {}^1I_{11/2}$ emission bands that are overwhelmed by background noise. In an independent measurement taken at 16-bit resolution, the characteristic time-decays for those weak lines were estimated, obtaining values ranging from 0.08 ms to 0.12 ms, suggesting that these transitions are overwhelmed by the noise in low-resolution images.

The onset of the time profiles can provide information about the multiphoton pathway by which the high-energy states are populated into the UCNP lattice. The sigmoid appearance of the initial rise is generated due to the time that is needed to populate first the intermediate energy states, which finally leads to the emissive ones Although a complete analysis of this information is somewhat beyond the scope of this work, the shape of these onsets could be used to differentiate pathways. However, a shorter timescale could be the best option to achieve this goal, since the population path seems to be faster than the emission mechanisms. Further work is focused on this aspect, with a slightly modified instrument capable of measuring at two timescales at a time.

3.4. Temperature dependence analysis.

The intensity of UCL is sensitive to several factors, such as the nature of the surface ligand, the surrounding medium, and the temperature. In this regard, the thermal dependence of the UCL has risen as attractive non-invasive thermometers for determining the temperature at nanoscales where conventional methods are neither suitable nor effective. [19,39] Er^{3+} ion is the most used lanthanide for temperature sensing-based techniques since the emission bands assigned to $^2H_{11/2} \rightarrow {}^4I_{15/2}$ and $^4S_{3/2} \rightarrow {}^4I_{15/2}$ radiative transitions, positioned at 520 nm and 540 nm, respectively, are thermally coupled and its relative emission intensity exhibit strong dependency with temperature, i.e., UCL quenching with raising the temperature. [10,17,18] However, it is known that not only the intensity but also the time-decay of UCL changes with this factor. This effect promotes the difficulty of manipulating the UCL time-decay in complex systems. Hence, to address this problem, at least two solutions can be proposed: 1) the synthesis of a new generation of independent time-decay UCNP, and 2) the development of new methodologies that enable the integral evaluation of the system. In this regard, it is a noteworthy fact that the instruments utilized for multiphoton spectroscopy are equipped with Ti-Sapphire lasers which are delicate, big, and expensive, which may be a reason for the low spread of this technology.

To assess the capability of the setup to monitor changes either in the emission spectrum or the time behaviour by external perturbations, EtMs at different temperatures were acquired as a proof of concept.

In a first attempt to evaluate the system, EtM at 3 different temperatures (297 K; 327 K, and 367 K) were individually analyzed through MCR-ALS, because both the spectral and the time curve would vary with the temperature. For the MCR-ALS

resolution, a SIMPLISMA-like methodology [37,38] was utilized to extract the initial estimates in the time mode and the number of components was estimated through SVD and PCA. During the iterative step, nonnegativity in both modes was imposed as a constraint. The retrieved profiles are depicted in Figure 4.

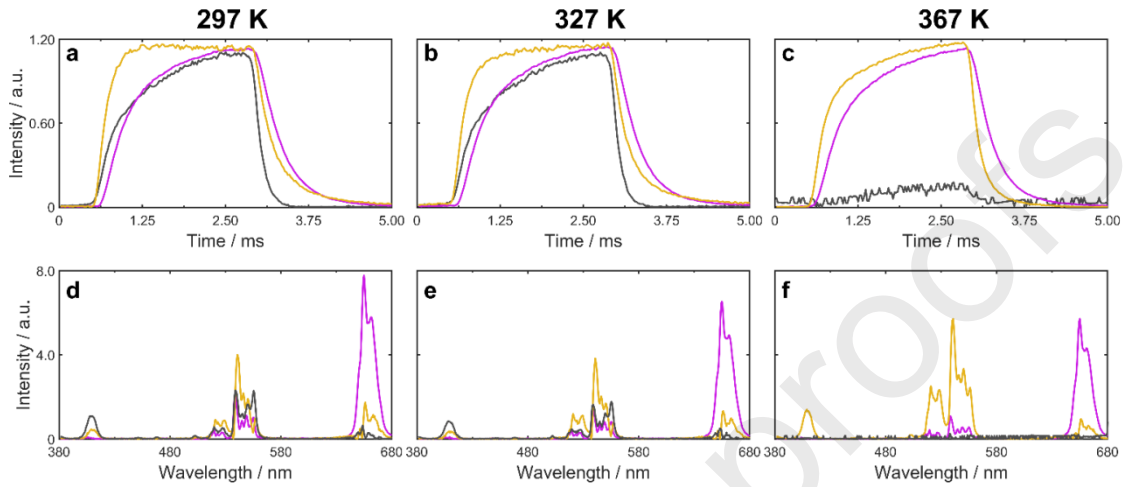

Figure 4. Time curve (top) and spectral (bottom) profiles achieved after MCR-ALS decomposition of 8-bit resolution EtM acquired at 297 K (a and d), 327 K (b and e), and 367 K (c and f). (Colour should be used in the print version)

Even though three components were necessary to explain the system in all cases, two main profiles represent the UC total system at 367 K. However, the time profile of the third component presents a slight feature, for which the signal-to-noise ratio does not allow the proper analysis of the results. As expected, the results demonstrated that both time and spectral features change with raising the temperature. On one hand, for the same component, both the rise and the decay region of the time curve featured differently with temperature variations. On the other, the spectral feature varies in dependence on the temperature Table 1 summarizes the τ-values calculated from the decayed part of the MCR-ALS time profiles obtained at different temperatures.

Table 1. τ-values obtained from the retrieved MCR-ALS profiles at different temperatures.

Component[1]	τ-values		
	297 K	327 K	367 K

1: magenta	0.38 ms	0.36 ms	0.33 ms
2: orange	0.30 ms	0.27 ms	0.18 ms
3: black	0.14 ms	0.14 ms	NC[2]

[1] Color is according to Figure 4.

[2] Not calculated

Shorter time-decays are obtained at higher temperatures. Nevertheless, the bands with shorter time-decays do not show variations in their τ-value while increasing the temperature, but their relative intensities are dramatically quenched, leading to a non-detected band at the highest temperature. In this regard, it can be appreciated that the intensity of some emission bands decreases with rising temperature, whereas others increase. Hence, to reinforce this observation, an emission-temperature matrix was built by stacking the emission spectra (at the end of the excitation pulse) acquired at different temperatures. At this point, it becomes mandatory to highlight the fact that, from the chemometric standpoint, a three-dimensional data array (emission-time-temperature) does not fulfil the concept of trilinearity due to the strong dependence between emission and time modes with temperature. In this way, a bilinear matrix of dimension 320 × 512 was obtained for temperature and emission wavelength, respectively, and was subjected to MCR-ALS decomposition. Results are shown in Figure 5.

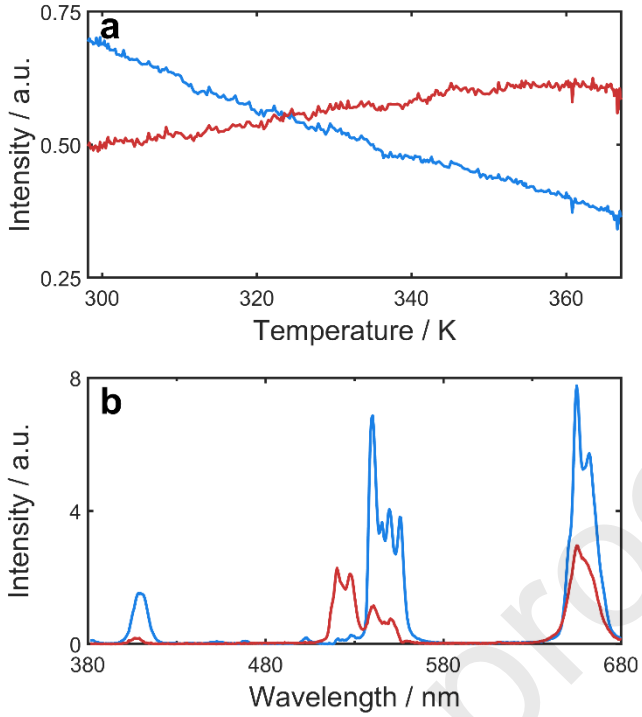

Figure 5. a) Temperature-dependence and b) spectral profiles achieved after MCR-ALS decomposition of an emission-temperature data matrix. (Colour should be used in the print version)

The two components that were necessary to explain the system present opposite trends against temperature. In comparison with Figure 4, the bands with a τ-value of about 0.30 ms (mainly present in the green band) rise while heating. On the contrary, the bands with longer and shorter time-decays (magenta and black in Figure 3) exhibit a thermal quenching yielding lower intensities at higher temperatures. This observation is in total agreement with Rabuffetti et al.,[24,25] where the authors demonstrated the temperature-dependence of $^{2}H_{11/2}$ and $^{4}S_{3/2}$ and the potential of the Er^{3+}-doped UCNPs as nanothermometers by measuring emission intensity and the emission time-decays.

4. CONCLUSIONS

A straightforward approach was developed for the characterization of UCNPs regarding their upconversion photoluminescence time behaviour at the entire emission spectrum by the acquisition of bidimensional emission wavelength-time matrices.

The effectiveness of the method was assessed by analysing the acquired signals through chemometric techniques. In all cases, the Er^{3+} emission bands were identified and could be associated with the corresponding energetic radiative transitions. In addition, not only the intensity but also their associated time curve was possible to determine. In this regard, one significant outcome of this work was the capability of the setup to detect weak emission bands with their associated time curves, such as those corresponding to

$^4F_{7/2} \rightarrow {}^4I_{15/2}$, $^4F_{5/2} \rightarrow {}^4I_{15/2}$ and $^2P_{3/2} \rightarrow {}^1I_{11/2}$ transitions, which are commonly not reported.

Moreover, the applicability of the developed method to monitor changes in the UC signals by external perturbations was stressed. Here, changes in the UC emission profiles and the time behaviour by increment in the surrounding temperature were monitored. Chemometric decomposition was implemented to gain comprehensive and meaningful information about the system. The results show that both emission and time profiles behave differently with temperature. The results align with the findings in the existing literature. An important aspect to highlight is the possibility of monitoring real-time signal variations due to the high scan rate of the detector.

Based on the obtained results, the presented approach becomes a valuable and powerful alternative to straightforwardly obtain comprehensive information about the temperature-dependency of time-decays and UC emission. The fibre-optics sensing element implies a very high versatility and portability allowing the simple and easy measurement of the entire spectrum and emission time dependence of UCNPs micro samples in difficult-to-access, chemically challenging, or hot environments, such as during the synthesis or derivatization procedures.

Moreover, it is important to note that with a simple change of the filters and dichroic mirror characteristics, the same procedure can be used for obtaining high-quality high-throughput data of other types of samples in which the time kinetics lies in the microsecond-millisecond range. This includes, among others, lanthanide emissions where upconversion processes are not involved.

Last, the combination of high-quality data acquisition with chemometrics aided in understanding better the phenomena occurring in the emission process.

AUTHOR CONTRIBUTIONS

Mirta Raquel Alcaraz: Data curation, Formal analysis, Investigation, Methodology, Software, Validation, Visualization, Writing - Original Draft, Writing – review & editing. Cecilia Sorbello: Investigation, Methodology, Validation, Writing – review & editing. Loreiny Parra Florez: Investigation, Methodology, Validation, Writing – review & editing. Roberto Etchenique: Conceptualization, Data curation, Formal analysis, Funding acquisition, Methodology, Supervision, Validation, Visualization, Writing - Original Draft, Writing – review & editing.

ACKNOWLEDGEMENTS

This research was supported by the ANPCyT (Agencia Nacional de Promoción Científica y Tecnológica, Project PICT-2017- 1494), CONICET (Consejo Nacional de Investigaciones Científicas y Técnicas) and the UBA (Universidad de Buenos Aires, Project: UBACYT 2018 20020170100295BA). MRA, CS, and RE are staff of CONICET. LPF thanks CONICET for the doctoral fellowship.

NOTES

All figures must be in colour in the print version.

REFERENCES

[1] J. Zhou, Q. Liu, W. Feng, Y. Sun, F. Li, Upconversion luminescent materials: advances and applications, Chem Rev. 115 (2015) 395–465. https://doi.org/10.1021/cr400478f.

[2] K.E. Sapsford, W.R. Algar, L. Berti, K.B. Gemmill, B.J. Casey, E. Oh, M.H. Stewart, I.L. Medintz, Functionalizing nanoparticles with biological molecules: Developing chemistries that facilitate nanotechnology, Chem Rev. 113 (2013) 1904–2074. https://doi.org/10.1021/cr300143v.

[3] Y. Wu, J. Xu, E.T. Poh, L. Liang, H. Liu, J.K.W. Yang, C.-W. Qiu, R.A.L. Vallée, X. Liu, Upconversion superburst with sub-2 μs lifetime, Nat Nanotechnol. 14 (2019) 1110–1115. https://doi.org/10.1038/s41565-019-0560-5.

[4] G. Chen, H. Qiu, P.N. Prasad, X. Chen, Upconversion Nanoparticles: Design, nanochemistry, and applications in theranostics, Chem Rev. 114 (2014) 5161–5214. https://doi.org/10.1021/cr400425h.

[5] S. Wu, H. Butt, Near-infrared-sensitive materials based on upconverting nanoparticles, Advanced Materials. 28 (2016) 1208–1226. https://doi.org/10.1002/adma.201502843.

[6] J. Bergstrand, Q. Liu, B. Huang, X. Peng, C. Würth, U. Resch-Genger, Q. Zhan, J. Widengren, H. Ågren, H. Liu, On the decay time of upconversion luminescence, Nanoscale. 11 (2019) 4959–4969. https://doi.org/10.1039/C8NR10332A.

[7] Y. Han, C. Gao, T. Wei, K. Zhang, Z. Jiang, J. Zhou, M. Xu, L. Yin, F. Song, L. Huang, Modulating the rise and decay dynamics of upconversion luminescence through controlling excitations, Angewandte Chemie International Edition. 61 (2022) e202212089. https://doi.org/https://doi.org/10.1002/anie.202212089.

[8] Y. Han, H. Li, Y. Wang, Y. Pan, L. Huang, F. Song, W. Huang, Upconversion modulation through pulsed laser excitation for anti-counterfeiting, Sci Rep. 7 (2017) 1320. https://doi.org/10.1038/s41598-017-01611-9.

[9] J. Hodak, Z. Chen, S. Wu, R. Etchenique, Multiphoton excitation of upconverting nanoparticles in pulsed regime, Anal Chem. 88 (2016) 1468–1475. https://doi.org/10.1021/acs.analchem.5b04485.

[10] M. Fernanda Torresan, J. Morrone, C. Sorbello, R. Etchenique, P.C. Angelomé, A. Wolosiuk, Emissive platforms employing $NaYF_4$-based upconverting nanoparticles and mesoporous metal oxide thin films, Eur J Inorg Chem. 2021 (2021) 2343–2352. https://doi.org/https://doi.org/10.1002/ejic.202100177.

[11] J. Shen, L. Zhao, G. Han, Lanthanide-doped upconverting luminescent nanoparticle platforms for optical imaging-guided drug delivery and therapy, Adv Drug Deliv Rev. 65 (2013) 744–755. https://doi.org/http://dx.doi.org/10.1016/j.addr.2012.05.007.

[12] A.D. Ostrowski, E.M. Chan, D.J. Gargas, E.M. Katz, G. Han, P.J. Schuck, D.J. Milliron, B.E. Cohen, Controlled synthesis and single-particle imaging of bright, sub-10 nm lanthanide-doped upconverting nanocrystals, ACS Nano. 6 (2012) 2686–2692. https://doi.org/10.1021/nn3000737.

[13] M.F. Torresan, L. Parra-Florez, C. Sorbello, J.C. Azcárate, R. Etchenique, A. Wolosiuk, Sodium hexametaphosphate: An inexpensive inorganic polyelectrolyte "primer" for upconverting nanoparticles/mesoporous silica core-shell synthesis, Chemistry Select. 5 (2020) 5210–5216. https://doi.org/https://doi.org/10.1002/slct.202000287.

[14] TheMathWorks, MATLAB R2015b, (2015).

[15] J. Jaumot, A. De Juan, R. Tauler, MCR-ALS GUI 2.0: New features and applications, Chemometrics and Intelligent Laboratory Systems. 140 (2015) 1–12. https://doi.org/http://dx.doi.org/10.1016/j.chemolab.2014.10.003.

[16] J. Zhao, Z. Lu, Y. Yin, C. McRae, J.A. Piper, J.M. Dawes, D. Jin, E.M. Goldys, Upconversion luminescence with tunable lifetime in $NaYF_4$:Yb,Er nanocrystals: role of nanocrystal size, Nanoscale. 5 (2013) 944–952. https://doi.org/10.1039/C2NR32482B.

[17] O.A. Savchuk, J.J. Carvajal, Y. Cesteros, P. Salagre, H.D. Nguyen, A. Rodenas, J. Massons, M. Aguiló, F. Díaz, Mapping temperature distribution generated by photothermal conversion in graphene film using Er,Yb:$NaYF_4$ nanoparticles prepared by microwave-assisted solvothermal method, Front Chem. 7 (2019). https://doi.org/10.3389/fchem.2019.00088.

[18] F. Vetrone, R. Naccache, A. Zamarrón, A. Juarranz de la Fuente, F. Sanz-Rodríguez, L. Martinez Maestro, E. Martín Rodriguez, D. Jaque, J. García Solé, J.A. Capobianco, Temperature sensing using fluorescent nanothermometers, ACS Nano. 4 (2010) 3254–3258. https://doi.org/10.1021/nn100244a.

[19] C.D.S. Brites, P.P. Lima, N.J.O. Silva, A. Millán, V.S. Amaral, F. Palacio, L.D. Carlos, Thermometry at the nanoscale, Nanoscale. 4 (2012) 4799–4829. https://doi.org/10.1039/C2NR30663H.

[20] D.R. Tallant, M.P. Miller, J.C. Wright, Energy transfer and relaxation phenomena in CaF_2:Er^{3+}, J Chem Phys. 65 (1976) 510–521. https://doi.org/10.1063/1.433130.

[21] D.S. Moore, J.C. Wright, Laser spectroscopy of defect chemistry in CaF_2:Er^{3+}, J Chem Phys. 74 (1981) 1626–1636. https://doi.org/10.1063/1.441303.

[22] J.M. Bujjamer, M. Claudia Marchi, B.C. Barja, H.E. Grecco, Luminescent materials as spectral converters: Power dependent profiling of solid $NaYF_4$:Yb^{3+}, Er^{3+} UCNP reveals highly efficient UVA–blue emission, Energy Reports. 6 (2020) 63–69. https://doi.org/https://doi.org/10.1016/j.egyr.2019.11.024.

[23] D.R. Tallant, J.C. Wright, Selective laser excitation of charge compensated sites in $CaF_2:Er^{3+}$, J Chem Phys. 63 (1975) 2074–2085. https://doi.org/10.1063/1.431545.

[24] S.S. Perera, K.T. Dissanayake, F.A. Rabuffetti, Alkaline-earth fluorohalide nanocrystals for upconversion thermometry, J Lumin. 207 (2019) 416–423. https://doi.org/https://doi.org/10.1016/j.jlumin.2018.11.036.

[25] B.D. Dhanapala, H.N. Munasinghe, F.A. Rabuffetti, Temperature-dependent luminescence of CaFCl:Yb,Er upconverting nanocrystals, J Lumin. 235 (2021) 117974. https://doi.org/https://doi.org/10.1016/j.jlumin.2021.117974.

[26] L.-Q. Xiong, Z.-G. Chen, M.-X. Yu, F.-Y. Li, C. Liu, C.-H. Huang, Synthesis, characterization, and in vivo targeted imaging of amine-functionalized rare-earth up-converting nanophosphors, Biomaterials. 30 (2009) 5592–5600. https://doi.org/https://doi.org/10.1016/j.biomaterials.2009.06.015.

[27] M. Dammak, D.L. Zhang, Spectra and energy levels of Er^{3+} in Er_2O_3 powder, J Alloys Compd. 407 (2006) 8–15. https://doi.org/10.1016/J.JALLCOM.2005.06.017.

[28] S. Ferber, V. Gaebler, H.J. Eichler, Violet and blue upconversion-emission from erbium-doped ZBLAN-fibers with red diode laser pumping, Opt Mater (Amst). 20 (2002) 211–215. https://doi.org/10.1016/S0925-3467(02)00064-2.

[29] D. Šević, M.S. Rabasović, J. Križan, S. Savić-Šević, M.D. Rabasović, B.P. Marinkovic, M.G. Nikolic, Effects of temperature on luminescent properties of Gd_2O_3:Er, Yb nanophosphor, Opt Quantum Electron. 52 (2020) 232. https://doi.org/10.1007/s11082-020-02348-y.

[30] Z. Zhu, Smartphone-based apparatus for measuring upconversion luminescence lifetimes, Anal Chim Acta. 1054 (2019) 122–127. https://doi.org/https://doi.org/10.1016/j.aca.2018.12.016.

[31] A. de Juan, R. Tauler, Multivariate Curve Resolution: 50 years addressing the mixture analysis problem - A review, Anal Chim Acta. 1145 (2021) 59–78. https://doi.org/10.1016/j.aca.2020.10.051.

[32] R. Tauler, M. Maeder, A. de Juan, 2.15 - Multiset Data Analysis: Extended Multivariate Curve Resolution, in: S. Brown, R. Tauler, B. Walczak (Eds.), Comprehensive Chemometrics, Second, Elsevier, Oxford, 2020: pp. 305–336. https://doi.org/https://doi.org/10.1016/B978-0-12-409547-2.14702-X.

[33] A. Schwaighofer, M.R. Alcaraz, L. Lux, B. Lendl, pH titration of β-lactoglobulin monitored by laser-based Mid-IR transmission spectroscopy coupled to chemometric analysis, Spectrochim Acta A Mol Biomol Spectrosc. 226 (2020) 117636. https://doi.org/10.1016/j.saa.2019.117636.

[34] M.R. Alcaraz, A.V.A. V Schenone, M.J.M.J. Culzoni, H.C. Goicoechea, M.R. Alcaraz, A.V.A. V Schenone, M.J.M.J. Culzoni, H.C. Goicoechea, Modeling of second-order spectrophotometric data generated by a pH-gradient flow injection technique for the determination of doxorubicin in human plasma, Microchemical Journal. 112 (2014) 25–33. https://doi.org/10.1016/j.microc.2013.09.012.

[35] M.R. Alcaraz, A. Schwaighofer, H. Goicoechea, B. Lendl, Application of MCR-ALS to reveal intermediate conformations in the thermally induced α-β transition of poly- l -lysine monitored by FT-IR spectroscopy, Spectrochim Acta A Mol Biomol Spectrosc. 185 (2017) 304–309. https://doi.org/10.1016/j.saa.2017.05.005.

[36] M.R. Alcaraz, A. Aguirre, H.C. Goicoechea, M.J. Culzoni, S.E. Collins, Resolution of intermediate surface species by combining modulated infrared spectroscopy and chemometrics, Anal Chim Acta. 1049 (2019). https://doi.org/10.1016/j.aca.2018.10.052.

[37] W. Windig, J. Guilment, Interactive self-modeling mixture analysis, Anal Chem. 63 (1991) 1425–1432. https://doi.org/10.1021/ac00014a016.

[38] W. Windig, A. Bogomolov, S. Kucheryavskiy, 2.08 - Two-Way Data Analysis: Detection of Purest Variables, in: S. Brown, R. Tauler, B. Walczak (Eds.), Comprehensive Chemometrics (Second Edition), Elsevier, Oxford, 2020: pp. 107–136. https://doi.org/https://doi.org/10.1016/B978-0-12-409547-2.14747-X.

[39] T.P. van Swieten, T. van Omme, D.J. van den Heuvel, S.J.W. Vonk, R.G. Spruit, F. Meirer, H.H.P. Garza, B.M. Weckhuysen, A. Meijerink, F.T. Rabouw, R.G. Geitenbeek, Mapping Elevated Temperatures with a Micrometer Resolution Using the Luminescence of Chemically Stable Upconversion Nanoparticles, ACS Appl Nano Mater. 4 (2021) 4208–4215. https://doi.org/10.1021/acsanm.1c00657.

HIGHLIGHTS

- Inexpensive setup for emission wavelength-time imaging
- UC luminescence behaviour at the entire emission spectrum
- Temperature dependence analysis of UC emission coupled with MCR-ALS
- MCR-ALS to solve overlapped spectral features

Declaration of interests

☒ The authors declare that they have no known competing financial interests or personal relationships that could have appeared to influence the work reported in this paper.

☐ The authors declare the following financial interests/personal relationships which may be considered as potential competing interests: